In Vivo-Informed CFD Suggests a New Mechanism for Syringomyelia Development in Chiari I Malformation

Francisco Javier Parras-Martos[1,6], Guillermo L. Nozaleda[2], Madison Sznicer[2], Wilfried Coenen[3], Carlos Martínez-Bazán[4,6], Vijay M. Ravindra[5], Allison Ludwick[5], Mandy Spear[5], John Rampton[5], Douglas Brockmeyer[5], Cándido Gutiérrez-Montes[1,6*], Antonio L. Sánchez[2*]

[1]Área de Mecánica de Fluidos, Departamento de Ingeniería Mecánica y Minera, Universidad de Jaén, Jaén, 23071, Spain.
[2*]Department of Mechanical and Aerospace Engineering, University of California San Diego, La Jolla, CA 92093-0411, USA.
[3]Departamento de Ingeniería Térmica y de Fluidos, Universidad Carlos III de Madrid, Leganés, 28911, Spain.
[4]Área de Mecánica de Fluidos, Departamento de Mecánica de Estructuras e Ingeniería Hidráulica, Universidad de Granada, Granada, 18071, Spain.
[5]Division of Pediatric Neurosurgery, Primary Children's Hospital, Salt Lake City, UT 84113, USA.
[6]Andalusian Institute for Earth System Research, Universidades de Granada, Córdoba y Jaén, Avenida del Mediterráneo s/n, Granada, 18006, Spain.

*Corresponding author(s). E-mail(s): cgmontes@ujaen.es; alsp@ucsd.edu;
Contributing authors: fjparras@ujaen.es; Guillermo.LopezNozaleda@childrens.harvard.edu; msznicer@ucsd.edu; wcoenen@ing.uc3m.es; cmbazan@ugr.es; Vijay.Ravindra@hsc.utah.edu; allison.ludwick@hsc.utah.edu; Mandy.Spear@imail.org; john.rampton@imail.org; Douglas.Brockmeyer@hsc.utah.edu;

Abstract

Chiari malformation type I (CM-I) is characterized by the descent of the cerebellar tonsils through the foramen magnum, partially obstructing the spinal canal and impeding the normal flow of cerebrospinal fluid (CSF) between the cranial and spinal compartments. A large fraction of patients with CM-I develop a syrinx, an intramedullary cavity filled with CSF. In response to cyclic variations in intracranial pressure, the tonsils oscillate and act effectively as a piston within the partially confined spinal subarachnoid space, displacing the cervical CSF immediately caudal to the tonsillar tips. It has been hypothesized that the resulting pulsatile pressure waves, with amplitudes on the order of a few pascals, disrupt normal transmedullary CSF exchange and promote a localized net inflow into the spinal cord, thereby contributing to syrinx formation. This hypothesis is revisited here using *in vivo*-informed numerical simulations of CSF flow in two pediatric patients with CM-I, one with a syrinx and one without. The computations, which explicitly account for the experimentally measured tonsillar motion, confirm the existence of the piston effect and further reveal the key role of the thin squeeze film separating the moving tonsils from the spinal cord. In particular, the overpressures required to expel the confined CSF during the downward motion of the tonsils, which scale inversely with the square of the film thickness, exceed the lower pressures required to replenish the gap during their upward motion. This asymmetry produces a net time-averaged squeeze-film overpressure whose magnitude, larger for the subject with a syrinx, exceeds by approximately two orders of magnitude that associated with the previously hypothesized piston effect. These steady overpressures may drive a localized net perivascular inflow from the squeeze film into the spinal cord at the foramen-magnum level. Once inside the cord, the resulting longitudinal pressure gradient could promote caudal flow and fluid accumulation below the region of tonsillar overpressure, consistent with progressive syrinx formation. Complementing the original piston theory, these findings further underscore the central role of tonsillar motion and suggest an additional syrinx-filling mechanism that may have been overlooked in previous studies.

Keywords: Biomedical fluid dynamics, Cerebrospinal fluid flow, Chiari malformation, Syringomyelia.

1 Background

Chiari malformation type I (CM-I) is a neurological condition in which the cerebellar tonsils, the lowermost structures of the cerebellum, descend through the foramen magnum into the upper spinal canal. As illustrated schematically in Fig. **??**a, this tonsillar herniation can substantially narrow or even occlude the cerebrospinal-fluid (CSF) passage at the craniocervical junction [**? ?**], thereby altering the normal communication between the cranial and spinal compartments and disrupting the oscillatory CSF motion driven by the cardiac and respiratory cycles in the spinal subarachnoid space (SSAS) [**?**]. A significant fraction of patients with CM-I also develop syringomyelia,

a condition characterized by the formation of a CSF-filled intramedullary cavity, or syrinx, most commonly within the cervical spinal cord.

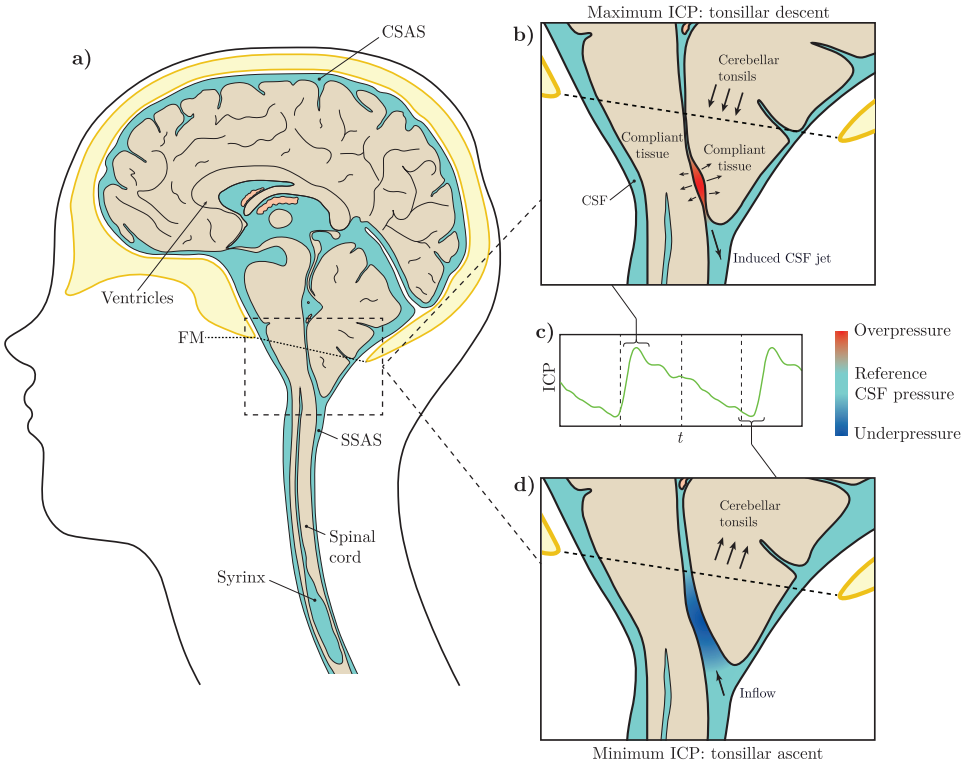

Fig. 1 Schematic representation of the craniocervical region of a subject with CM-I and syringomyelia. a) MRI-informed illustration of the upper spinal canal together with the cranial cavity of the studied subject 1 (see section **??**). b) Representation of the descending tonsillar motion (systolic pulse) and the associated dilation of the squeezing CSF film due to the compliance of the surrounding tissues. c) Temporal evolution of intracranial pressure, indicating the instants of tonsillar ascent (diastole) and descent (systole). d) Representation of the ascending tonsillar motion and the shape recovery of the herniated tonsils and spinal cord.

The mechanisms by which syrinxes originate and progress in patients with CM-I remain incompletely understood [**? ? ? ?**], although there is broad consensus that fluid accumulation is closely linked to the alterations in CSF flow, and associated pressure variations, caused by the tonsillar obstruction. Current theories point to deregulation of the normal transmedullary flow as the underlying mechanism explaining syrinx development [**? ? ? ? ?**]. In a healthy subject, there is a balance between transmedullary CSF inflow, occurring mainly through the perivascular spaces surrounding penetrating arteries [**?**], and the accompanying outflow. Changes in the SSAS pressure associated with CM-I may disrupt this bidirectional exchange, leading to fluid accumulation within the spinal cord.

This idea is present in the seminal theory of Oldfield et al. [**?**]. They noted that the intracranial pressure (ICP) fluctuations responsible for the pulsating motion of CSF across the foramen magnum (FM) in healthy subjects with an unobstructed SSAS exert a cyclic force on the tonsils plugging the posterior SSAS of CM-I patients. The resulting piston-like tonsillar motion, which has been quantified in recent magnetic resonance imaging (MRI) studies [**? ?**], generates a pressure wave in the spinal CSF caudal to the tonsils, which may alter the transmedullary flow balance and thereby contribute to the origin of the syrinx [**? ? ? ?**]. As noted by Oldfield et al. [**?**], once syringomyelia develops, the SSAS pressure wave induces a sloshing motion within the cavity [**? ?**] that may further contribute to its growth, an aspect of the problem that has been the subject of numerical [**? ? ? ? ?**], experimental [**?**], and analytic [**?**] investigations. More recently, Lloyd et al. [**?**] complemented the piston theory by noting that phase changes in the SSAS pressure wave of CM-I patients may have an important effect on the resulting periarterial inflow, whose net value depends critically on the relative timing of the arterial and SSAS pulse waves [**?**].

While previous theories have emphasized the key role of piston-like tonsillar motion in disrupting transmedullary flow by altering the magnitude and phase of the pressure wave along the SSAS immediately caudal to the tonsillar tips [**? ? ? ? ?**], they appear to have largely overlooked the pressure variations occurring within the *tonsillomedullary film* (TMF), defined here as the thin layer of CSF bounded posteriorly by the anterior surface of the cerebellar tonsils and anteriorly by the posterior surface of the spinal cord/medulla. As shown in Fig. **??**b, as the tonsils move downward with each systolic pulse (Fig. **??**c), the TMF is squeezed, generating a rapid CSF ejection below the level of obstruction. Conversely, as the tonsils retreat during diastole (Fig. **??**c), CSF moves upward to fill the widening gap, as represented in Fig. **??**d. The presence of this systolic jet was mentioned briefly by Oldfield et al. [**?**]—see the small inset in the bottom right corner of their figure 3a and the accompanying comment in the figure caption—but its potential significance was not analyzed in detail.

Unlike the flow in the relatively wide SSAS, which is characterized by weak viscous effects [**?**], the dynamics of the TMF, whose width is submillimetric, can be expected to be fundamentally an unsteady lubrication problem, largely dominated by viscous forces. During systolic downward tonsillar motion, a large overpressure builds up within the gap, as needed to expel fluid into the spinal canal. Conversely, during diastolic upward motion of the tonsils, the pressure within the gap must become negative relative to its mean value, drawing CSF back into the widening film. The amplitude of the associated pressure oscillations scales inversely with the square of the film thickness, as follows from a balance between viscous and pressure forces.

An important observation is that the periodic viscous flow arising in the TMF is analogous to that encountered in vibration-driven squeeze-film systems, which have been extensively studied in connection with near-field acoustic levitation, non-contact transport, and squeeze-film bearings [**? ? ?**]. As shown in recent theoretical work [**?**], the periodic pressure along the film generally exhibits a nonzero cycle-averaged component, which can be either positive or negative. In fluid films bounded by deformable solids, the resulting dynamics depends strongly on the underlying fluid–structure interactions, which can give rise to significant net overpressures [**?**]. Since the fluid film

considered here is bounded by the compliant surfaces of the spinal cord and the tonsils, similar overpressures can be expected to develop as a result of the cyclic tonsillar displacement. This aspect of the problem, overlooked in previous studies, is the focus of the present work, which uses *in vivo*-informed computational fluid dynamics (CFD) simulations to evaluate the associated pressure field.

CFD studies incorporating different levels of patient-specific information have been instrumental in clarifying various aspects of cervical CSF flow dynamics in CM-I patients [**? ? ? ? ? ? ? ? ? ? ? ?**]. When combined with MRI-derived anatomical and flow data, CFD enables the full reconstruction of volumetric, time-resolved velocity fields, together with the noninvasive estimation of pressure fields, information that would otherwise be inaccessible without lumbar puncture [**?**]. Thus, *in vivo*-informed CFD simulations provide an attractive strategy for a preliminary assessment of the piston effect in CM-I patients, including the pressure induced in the SSAS immediately caudal to the tonsillar tips and in the TMF. To that end, we use T2-weighted anatomical data and phase-contrast MRI (PC-MRI) flow velocities from two pediatric CM-I patients with different degrees of craniocervical obstruction, one with a syrinx and one without. The CFD simulations, which incorporate cyclic tonsillar displacement as well as a Winkler approximation [see **?** , for details] to describe the fluid–structure interactions (FSI) occurring in the TMF, are used to compute pressure fluctuations and associated time-averaged pressure distributions. The results reveal large net overpressures along the TMF, with increasing magnitudes for decreasing film thicknesses. We argue that these time-averaged overpressures may promote transmedullary inflow at the FM level, followed by longitudinal intramedullary flow, thereby providing a possible mechanism for syrinx formation at a distant caudal location that complements the original piston theory.

2 Methods

2.1 Patient cohort

The study population consisted of two pediatric patients with CM-I: a 14-year-old female with associated syringomyelia (subject 1) and a 17-year-old female without syringomyelia (subject 2). A sagittal view of the craniocervical region corresponding to subject 1 is shown in Fig. **??**a. All experimental procedures were approved by University of Utah and Intermountain Institutional Review Boards (IRB_00178613). Prior to participation, written informed consent was obtained from the parents or legal guardians of both subjects, and assent was obtained from both subjects. The study was conducted in accordance with the relevant guidelines and regulations.

2.2 Magnetic resonance imaging

MRI was performed on a 3T GE Architect scanner equipped with software version MR30.1. Anatomical images of the craniocervical region were acquired using a three-dimensional sagittal T2-weighted Cube sequence with fat suppression. Imaging was performed with a 19-channel head-and-neck coil, used in combination with a 40-channel GEM posterior array coil for coverage of the remaining spine. For both

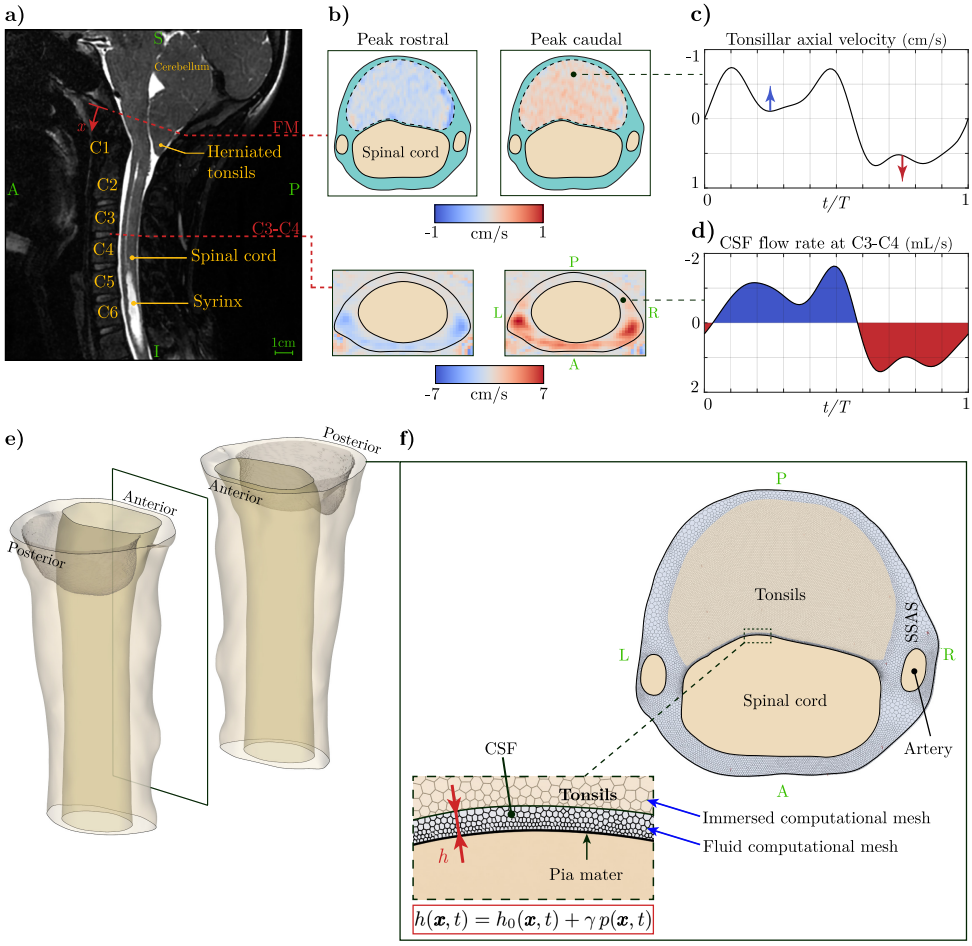

Fig. 2 Overview of the MRI data, velocity measurements and computational geometry for subject 1; velocities refer to the component along the direction perpendicular to the measurement plane, with a positive magnitude indicating craniocaudal motion. a) Sagittal MRI view showing the herniated tonsils and a syrinx. b) Tonsillar velocity distribution at the FM level (first row) and CSF velocity distribution at the C3–C4 vertebral level (second row), both at the instants of peak rostral tonsillar velocity (first column) and peak caudal tonsillar velocity (second column). c) Spatially averaged tonsillar velocity. d) CSF flow rate at the C3–C4 vertebral level. e) Posterior and anterior views of the segmented geometry, including the herniated tonsils. f) FM boundary of the generated computational mesh, together with a detail of the TMF.

subjects, imaging parameters were flip angle = 90°, matrix size 512 × 512, and slice thickness 0.8 mm. For subject 1, TR = 1502 ms, TE = 122.8 ms, and in-plane resolution was 0.469×0.469 mm^2. For subject 2, TR = 1500 ms, TE = 123.1 ms, and in-plane resolution was 0.429×0.429 mm^2.

Cardiac-gated two-dimensional PC-MRI acquisitions were performed at two axial locations of the cervical canal. One acquisition was positioned at the FM and was used to characterize cerebellar tonsillar motion, whereas a second acquisition was

positioned at the C3–C4 level and was used to characterize oscillatory CSF flow. The PC-MRI sequence employed through-plane velocity encoding. Imaging parameters included TR = 27.0 ms, flip angle = 10°, matrix size 512 × 512, in-plane resolution 0.391 × 0.391 mm^2, slice thickness 4 mm, and 30 reconstructed cardiac phases per cardiac cycle. The physiological condition during image acquisition was free-breathing with no sedation. Cardiac synchronization was achieved using peripheral pulse gating, corresponding to retrospective cardiac gating. For the foramen-magnum acquisition, the encoding velocity was set to VENC = 5 cm/s. For subject 1, the echo time was TE = 9.35 ms, and for subject 2, the echo time was TE = 9.25 ms. For the C3–C4 acquisition, the encoding velocity was set to VENC = 10 cm/s. For subject 1, the echo time was TE = 8.21 ms, and for subject 2, the echo time was TE = 8.22 ms. The heart rates recorded during the acquisitions were 93 bpm for both the FM and C3–C4 measurements in subject 2. For subject 1, the heart rates recorded during the FM and C3–C4 acquisitions were 105 bpm and 98 bpm, respectively.

2.3 Measurement of oscillatory CSF and tonsillar velocities

Oscillatory CSF flow and cerebellar tonsillar motion were quantified from PC-MRI measurements acquired at the C3–C4 and FM levels, respectively. Following the methodology described in our previous study [**?**], raw phase and magnitude images were processed using an in-house MATLAB code to extract the velocity component normal to the imaging plane throughout the cardiac cycle. Manually segmented regions of interest were used to extract the pixel-wise velocity field from the phase-contrast data. Spatial filtering, outlier removal, and phase-unwrapping procedures were subsequently applied to reduce measurement artifacts and correct for velocity aliasing. The resulting instantaneous velocity fields at peak rostral and caudal flow are shown in Fig. **??**b for subject 1.

The time-resolved velocity at each pixel j was temporally filtered by retaining Fourier harmonics up to order 10, yielding

$$u_j(t) = \sum_{k=-10}^{10} c_{j,k} \exp\left(\frac{2\pi \mathrm{i} k t}{T}\right), \tag{1}$$

where T is the cardiac period and $c_{j,k}$ are the complex Fourier coefficients associated with pixel j and mode k.

At the FM level, the cerebellar tonsils were manually segmented on the PC-MRI images. The corresponding tonsillar velocity waveform was obtained by spatially averaging the reconstructed through-plane velocity over the segmented tonsillar region according to

$$\bar{u}_{\mathrm{t}}(t) = \frac{\sum_{j=1}^{N_{p,t}} u_j(t)\, A_j}{\sum_{j=1}^{N_{p,t}} A_j}, \tag{2}$$

where $N_{p,t}$ denotes the number of pixels contained within the tonsillar region and A_j denotes the area of pixel j. The resulting waveform for subject 1 is shown in Fig. **??**c.

Similarly, at the C3–C4 level, the CSF region was manually segmented from the PC-MRI images. The reconstructed velocity field $u_j(t)$, to be used as a boundary

condition in the numerical simulations, was integrated over the segmented CSF area to yield the cyclic volumetric-flow-rate variation

$$Q_{\mathrm{CSF}}(t) = \sum_{j=1}^{N_{p,c}} u_j(t)\, A_j, \tag{3}$$

where $N_{p,c}$ denotes the number of pixels contained within the segmented CSF space. The flow rate for subject 1 is shown in Fig. **??**d.

2.4 A model of the craniocervical region

The computational domain, extending from the FM to the C3–C4 intervertebral level, was reconstructed using anatomical MRI data. The imaging data were semiautomatically segmented using ITK-SNAP (version 4.2.0; www.itksnap.org; [**?**]) and 3D Slicer [**?**]. Microanatomical features, such as nerve roots, denticulate ligaments and arachnoid trabeculae, were not segmented. Although these structures have been shown to be important in connection with transport in the spinal canal [**? ? ?**], their influence on the flow characteristics in the spinal region investigated here is anticipated to be moderately small. The segmentation process yielded an STL file that represents the entire CSF domain, bounded by the dura mater, the pia mater and the herniated cerebellar tonsils, with the vertebral arteries crossing the SSAS at the FM level. Subsequently, surface smoothing was applied to remove nonphysical irregularities. The resulting geometries—shown in Fig. **??**e and the rightmost panel of Fig. **??**a for subject 1 and in the rightmost panel of Fig. **??**a for subject 2—exhibit total lengths of 6.2 cm (subject 1) and 5.6 cm (subject 2), with total CSF and tonsillar volumes of 6.61 mL and 1.05 mL, respectively, for subject 1 and 6.17 mL and 0.616 mL, respectively, for subject 2.

The cervical geometry of the spinal canal was used as input to generate a computational unstructured mesh, based on polyhedra, using ANSYS Fluent Meshing (2023 R1; Ansys Inc., Pennsylvania). As seen in Fig. **??**f, polyhedral cells are distributed both in the CSF-filled space, delimited by the pia mater, the dura mater and the vertebral arteries, and inside the herniated tonsils, which are treated as a rigid solid. A mesh sizing control of 0.1 mm was imposed over the main walls, to ensure a correct description of the near-wall flow dynamics. Across the TMF, the cell size was reduced to 6.66 μm, as needed to enable the FSI scheme (see Fig. **??**f and section **??**). Finally, iterative remeshing was applied to provide sufficient orthogonality for increased numerical accuracy. The resulting mesh had 9.12×10^6 cells and 45.6×10^6 faces for subject 1 and 7.37×10^6 cells and 38.1×10^6 faces for subject 2.

2.5 Numerical model and fluid–structure interaction formulation

The numerical integrations employed the commercial finite-volume solver ANSYS Fluent (2023 R1; Ansys Inc., Pennsylvania), with the SIMPLE (Semi-Implicit Method for Pressure-Linked Equations) algorithm used for velocity-pressure coupling with second-order accuracy in both space and time. CSF is considered as a Newtonian fluid

with density $\rho \simeq 1000\,\mathrm{kg/m^3}$ and kinematic viscosity $\nu \simeq 0.7 \times 10^{-6}\,\mathrm{m^2/s}$ [**?** **?** **?**]. The periodic flow is determined by the integration of the continuity and momentum equations

$$\nabla \cdot \boldsymbol{v} = 0, \quad \frac{\partial \boldsymbol{v}}{\partial t} + \boldsymbol{v} \cdot \nabla \boldsymbol{v} = -\frac{1}{\rho}\nabla p + \nu \nabla^2 \boldsymbol{v}, \tag{4}$$

where $\boldsymbol{v}$ is the velocity and p represents the static pressure referenced to that existing across the FM cross section.

The boundary conditions include no-slip on all solid boundaries, along with a condition of uniform pressure across the upper boundary at the FM level. The PC-MRI measurements across the C3–C4 vertebral section, shown for subject 1 in the bottom panels of Fig. **??**b, were used to define the boundary velocity distribution across the lower boundary. In the computations, the tonsils move periodically as rigid solids with the space-averaged velocity determined from the PC-MRI measurements, shown in Fig. **??**c for subject 1. In prescribing this motion, the minimum separation distance between the anterior tonsillar surface and the pia mater, achieved when the tonsils reach their lowest caudal position, was set to 30 μm. The tonsillar motion was implemented numerically using an immersed-boundary method (IBM) based on volumetric penalization [**?**].

The squeeze-film dynamics involves large pressure fluctuations that are expected to produce non-negligible deformations of the spinal and tonsillar tissues. In the numerical simulations, this effect is described using a Winkler approximation [**?**], a model widely used to represent the deformation of solids separated by thin fluid films [**?**]. The model assumes that the tissue-surface displacement is linearly proportional to the local pressure, $\delta(\boldsymbol{x}, t) = \gamma p(\boldsymbol{x}, t)$. For simplicity in the numerical implementation, the displacement was applied only to the spinal-cord surface. As a result, the local width of the TMF, $h(\boldsymbol{x}, t)$, differs from its rigid-surface value, $h_0(\boldsymbol{x}, t)$, according to

$$\delta(\boldsymbol{x}, t) = h(\boldsymbol{x}, t) - h_0(\boldsymbol{x}, t) = \gamma\, p(\boldsymbol{x}, t). \tag{5}$$

The compliance factor γ was introduced as an effective, lumped Winkler compliance for the combined deformation of the spinal cord and tonsillar tissues, rather than as a material property of either tissue alone. This treatment follows the Winkler-foundation approximation reviewed by **?**], where the normal deformation of a compliant substrate is represented through a local proportionality between pressure and normal displacement. The tissue stiffness was based on the kilopascal-scale cerebellar modulus reported by **?**], and a representative Young's modulus of 5 kPa was adopted. Brain tissue was treated as nearly incompressible by taking the Poisson's ratio as 0.496, consistent with the value reported for wet brain tissue by **?**]. Because the deformation considered here is predominantly normal and laterally constrained, the Young's modulus was converted to the corresponding constrained modulus, following a one-dimensional interpretation [**?** **?**], yielding a value of $E_c \simeq 200$ kPa. This constrained modulus was then combined with an effective length of approximately $d = 10$ mm, representing the typical width of the spinal cord and the herniated tonsils. This gives the adopted Winkler compliance $\gamma = d/E_c = 5 \times 10^{-8}$ m/Pa. The chosen value therefore represents the lumped normal compliance of a soft, nearly incompressible, millimeter-scale tissue region. It implies normal displacements of approximately 30 μm

for pressure changes of 0.6 kPa, which are small compared with the overall cerebellar dimensions but large enough to affect the local TMF thickness.

The fluid–structure interaction problem was solved by means of an iterative cycle-to-cycle procedure. A time-implicit formulation with second-order accuracy in space and time was used. Each cycle was divided into 100 time steps, with 40 iterations performed at each time step. The pressure and velocity fields were initialized to zero at the beginning of the simulation. The variation in the gap thickness h determined from (**??**) was accommodated by displacing the pia mater, which required the use of a dynamic mesh scheme. Convergence was reached after 15 cycles, once the maximum differences in the pressure field and in the time-dependent deformation between consecutive cycles became negligible. The same procedure can be used for both small and large deformations, provided that the relaxation factors are adjusted appropriately to prevent numerical oscillations. The numerical method was validated by computing the pressure field and wall deformation in a geometrically simple, compliant squeeze-film configuration and comparing the results with the corresponding quasi-analytical predictions of lubrication theory, as detailed in the Supplementary Material (Additional file 1).

For the rigid-wall problem, the temporal and spatial resolutions required to obtain mesh- and time-step-independent solutions had already been validated in a previous study [**?**]. Accordingly, the present simulations used time-step and mesh-size values equal to or smaller than those previously established to ensure numerical convergence. Since the tonsillar motion introduced here had not been considered in that previous study, an additional mesh-sensitivity study was performed for the coupled problem using a refined mesh in the TMF with the same characteristics but twice the number of polyhedral cells. To quantify the mesh dependence, the pressure field was examined over all time instants, and the field corresponding to the instant of maximum absolute pressure was selected. The pressure was then spatially averaged over the points belonging to the TMF. The relative difference between the baseline and refined mesh was 0.8%, thereby demonstrating that the mesh employed in this study is sufficiently accurate for predictive purposes.

3 Discussion of illustrative results

The CSF flow and associated pressure fluctuations in the craniocervical region were computed for the two subjects investigated here. The results, discussed below, highlight the importance of TMF dynamics.

3.1 Patient-specific oscillatory pressure dynamics

Representative results characterizing the oscillatory dynamics over the cycle are shown in Figs. **??** and **??** for subjects 1 and 2, respectively. As the tonsils move, they descend into the spinal canal, altering both the cross-sectional area available for CSF flow at the FM and their position relative to the pia mater. The resulting changes in canal morphology are illustrated in the upper panels of Figs. **??**a and **??**a, which show transverse views at the FM at three representative instants. The corresponding pressure distributions over the spinal-cord surface are shown in the lower panels.

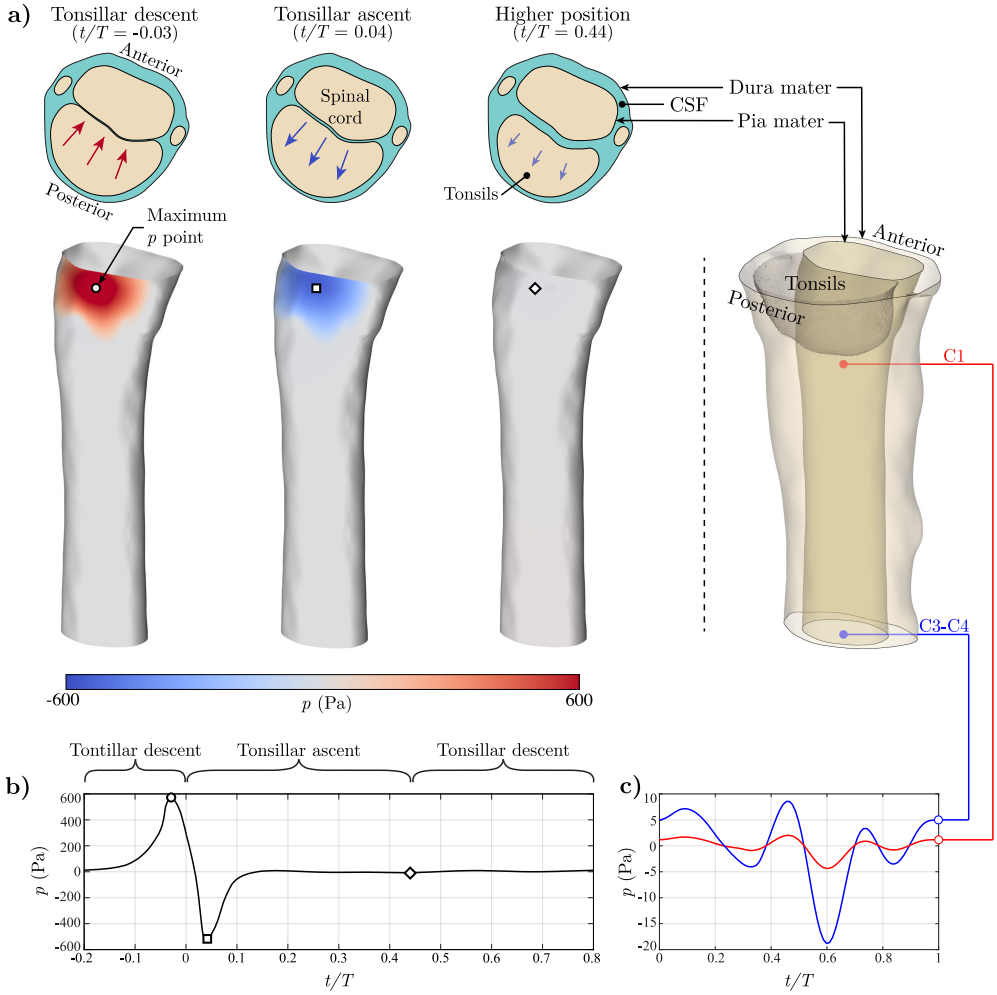

Fig. 3 Oscillatory static pressure dynamics for subject 1, who presents CM-I with associated syringomyelia. a) Transverse view at the FM level showing the spinal cord, the herniated cerebellar tonsils, the vertebral arteries, and the SSAS at three representative instants of the cycle: closest approach of the tonsils to the spinal cord, onset of tonsillar separation, and maximum separation, shown in the upper panel; spatial distribution of the static pressure over the pia mater at the three instants indicated in the upper panel, shown in the lower-left panel; and posterior view of the segmented geometry, including the herniated tonsils, shown in the rightmost panel. The circle, square, and diamond identify, respectively, the point of maximum pressure in the pia mater pressure contours and the corresponding positions in panel b) for the three representative instants described above. b) Temporal evolution of the static pressure at the point of maximum pressure in the TMF. c) Temporal evolution of the static pressure at the C1 and C3–C4 levels.

The first instant corresponds to the closest approach of the tonsils to the spinal cord, when the pressure within the TMF reaches its maximum. The second corresponds to the subsequent separation phase of the tonsils from the spinal cord, when the

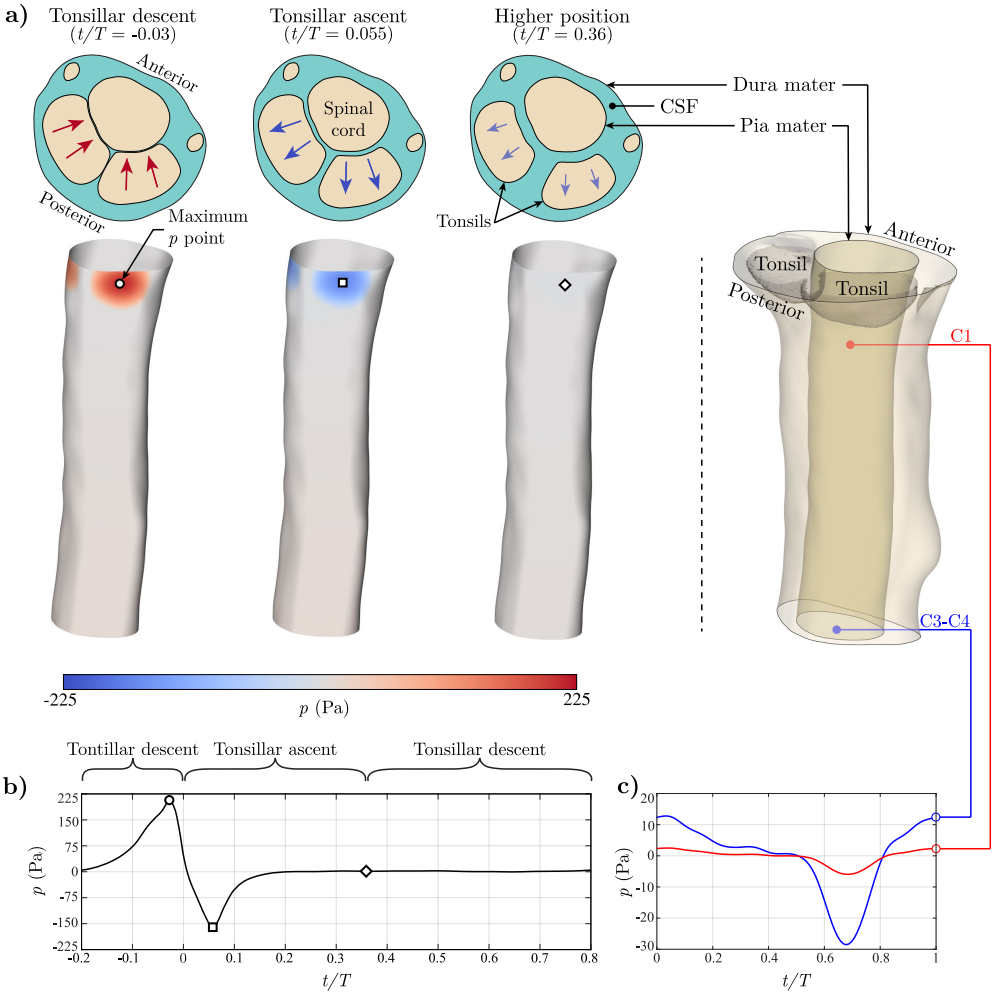

Fig. 4 Same as Fig. **??**, but for subject 2, who presents CM-I without associated syringomyelia.

minimum pressure occurs in the TMF. The final instant corresponds to a configuration in which the tonsils are farther from the spinal cord and the CSF pressure within the film is comparatively low.

This behavior is further illustrated in Figs. **??**b and **??**b, which show the evolution of the static pressure at a fixed point within the TMF, indicated by symbols in Figs. **??**a and **??**a. The magnitude of the pressure fluctuations within the TMF can be compared with that of the pressure wave generated caudally by the tonsillar motion. The dynamics of this spinal-pressure wave is characterized in Figs. **??**c and **??**c through the static-pressure histories at two representative locations corresponding to the C1 and C3–C4 vertebral levels.

As can be seen, the pressure fluctuations within the TMF (Figs. **??**b and **??**b) are much larger than those in the unobstructed SSAS (Figs. **??**c and **??**c), reflecting the fundamentally different nature of the underlying flows. This distinction can be clarified through an order-of-magnitude analysis of the momentum equation, given in Eq. (**??**). In the unobstructed SSAS, characterized by transverse dimensions $h_{\text{SSAS}} \sim 2$–4 mm, streamwise lengths $L_{\text{SSAS}} \sim 3$ cm, and velocities $u_{\text{SSAS}} \sim 5$ cm/s, comparison of the local acceleration $\partial \boldsymbol{v}/\partial t$ with the convective acceleration $\boldsymbol{v} \cdot \nabla \boldsymbol{v}$ and the viscous force per unit mass $\nu \nabla^2 \boldsymbol{v}$ gives

$$\frac{O(\boldsymbol{v} \cdot \nabla \boldsymbol{v})}{O(\partial \boldsymbol{v}/\partial t)} \sim \frac{u_{\text{SSAS}}}{\omega L_{\text{SSAS}}} \sim 0.166 \ll 1, \tag{6}$$

and

$$\frac{O(\nu \nabla^2 \boldsymbol{v})}{O(\partial \boldsymbol{v}/\partial t)} \sim \frac{\nu}{\omega h_{\text{SSAS}}^2} \sim 0.004 - 0.017 \ll 1 \tag{7}$$

where the inverse of the cardiac angular frequency $\omega = 2\pi/T$, which takes the value $\omega \simeq 10\ \text{s}^{-1}$ for the typical periods $T \sim 0.6 - 0.7$ s of our pediatric patients, has been used to characterize the local acceleration. The above orders of magnitude reveal that the dynamics of the piston-induced pressure wave is largely determined by the reduced equation

$$\frac{\partial \boldsymbol{v}}{\partial t} = -\frac{1}{\rho} \nabla p. \tag{8}$$

The associated order-of-magnitude balance $\partial \boldsymbol{v}/\partial t \sim -\nabla p/\rho$ yields

$$(\Delta p)_{\text{SSAS}} \sim \rho u_{\text{SSAS}} \omega L_{\text{SSAS}} \sim 15\ \text{Pa}, \tag{9}$$

in agreement with the computational results shown in Figs. **??**c and **??**c.

The balance equation (**??**) can be integrated over the spinal-canal cross section to yield

$$\frac{\partial Q}{\partial t} = -\frac{A}{\rho} \frac{\partial p}{\partial x}, \tag{10}$$

where $A = A(x)$ denotes the cross-sectional area of the SSAS. The validity of this relation for describing the pressure-wave dynamics in this region can be verified using the flow-rate history $Q(t)$ for subject 1, shown in Fig. **??**d, together with the corresponding pressure histories at C1 and C3–C4 shown in Fig. **??**c. As predicted by Eq. (**??**), the pressure gradient vanishes (i.e. $p_{\text{C1}} = p_{\text{C3-C4}}$) at the six instants for which $\partial Q/\partial t = 0$. Likewise, the maximum pressure difference, $(p_{\text{C1}} - p_{\text{C3-C4}})_{\max}$, occurs at $t/T = 0.6$, coinciding with the maximum rate of change of the flow rate, $(\partial Q/\partial t)_{\max}$, in Fig. **??**d. This instant corresponds to the transition from diastole to systole.

The flow dynamics within the TMF is markedly different. The film is characterized by transverse dimensions $h_{\text{TMF}} \ll h_{\text{SSAS}}$ and streamwise lengths $L_{\text{TMF}} \sim 1$ cm. The relative motion of its bounding surfaces, with transverse velocities of order ωh_{TMF}, generates longitudinal velocities of order $u_{\text{TMF}} \sim \omega L_{\text{TMF}}$, as follows from continuity.

Using this estimate in the momentum equation gives

$$\frac{O(\partial \boldsymbol{v}/\partial t)}{O(\nu \nabla^2 \boldsymbol{v})} \sim \frac{O(\boldsymbol{v} \cdot \nabla \boldsymbol{v})}{O(\nu \nabla^2 \boldsymbol{v})} \sim \frac{\omega h_{\text{TMF}}^2}{\nu}, \tag{11}$$

revealing that the flow dynamics in this region depends critically on the film thickness h_{TMF}. According to (**??**), for the small values $h_{\text{TMF}} \ll \sqrt{\nu/\omega} \sim 0.25$ mm that characterize the near-contact dynamics, viscous forces dominate. The resulting pressure fluctuations are therefore of order

$$(\Delta p)_{\text{TMF}} \sim \rho \nu \omega \left(\frac{L_{\text{TMF}}}{h_{\text{TMF}}} \right)^2, \tag{12}$$

as follows from the lubrication balance $\nu \nabla^2 \boldsymbol{v} \sim -\nabla p/\rho$. Thus, the pressure difference required to drive the fluid back and forth through the squeezed film scales with the square of the film aspect ratio, $L_{\text{TMF}}/h_{\text{TMF}}$. For example, aspect ratios $L_{\text{TMF}}/h_{\text{TMF}} = (200, 300)$ yield peak pressures $(\Delta p)_{\text{TMF}} \simeq (280, 630)$ Pa, consistent with the values shown in Figs. **??**b and **??**b.

Because of the inverse-square dependence on the film thickness displayed in Eq. (**??**), the squeezed-film effect becomes more pronounced as the tonsils approach the spinal cord. Accordingly, significant pressure fluctuations, of the order of hundreds of pascals, occur only over a short interval $-0.1 < t/T < 0.1$, centered about the instant of maximum proximity, $t = 0$. Outside this interval, the pressure fluctuations within the TMF are much smaller, as shown in Figs. **??**b and **??**b.

A comparison of the two subjects further reveals that the peak pressure reaches approximately 600 Pa in subject 1, compared with 225 Pa in subject 2. This difference can be attributed to variations in the morphology of the herniated tonsils. Subject 1 exhibits a severe obstruction, with the two tonsils appearing nearly fused, whereas subject 2 presents a milder obstruction, with the tonsils remaining separated and clearly distinguishable throughout the cycle. In addition, the tonsillar cross-sectional area shown in Fig. **??**a is smaller than that shown in Fig. **??**a. Consequently, although the tonsil—spinal-cord separation, characterized by the function $h(\boldsymbol{x}, t)$ in Eq. (**??**), is similar in the two subjects, these morphological differences—in particular, the much larger value of L_{TMF} in subject 1—are sufficient to produce substantially larger overpressures acting over a broader surface area, as shown by the pressure contours in the lower-left panel of Figs. **??**a and **??**a. Consistent with the respective tonsillar morphologies, two distinct regions of overpressure can be identified in subject 2, each associated with one cerebellar tonsil, whereas subject 1 exhibits a single, broader region of influence, consistent with the nearly fused tonsils behaving as a single entity.

3.2 Time-averaged pressure in the craniocervical region

The above computations reveal that the pressure field in the cervical spinal canal of patients with CM-I exhibits large temporal fluctuations synchronized with tonsillar motion, with magnitudes of a few tens of pascals in the unobstructed SSAS and a few hundred pascals in the TMF. Alterations in the pressure dynamics of the unobstructed

SSAS—that is, changes in pressure-wave amplitude and phase relative to those in healthy subjects—have been proposed to play a significant role in the inception and development of syringomyelic cavities [**? ? ? ?**]. There is also interest in determining whether the tonsillar piston effect produces changes in the associated time-averaged pressure

$$\langle p \rangle = \frac{1}{T} \int_t^{t+T} p \, \mathrm{d}t. \tag{13}$$

The underlying hypothesis is that elevated pressures in the SSAS could increase CSF inflow through the periarterial spaces of the spinal cord [**? ?**] while correspondingly reducing outflow along the perivenous spaces, thereby disrupting the normal balance between transmedullary inflow and outflow. If compensatory CSF-removal mechanisms, such as longitudinal flow along the spinal-cord central canal, are unable to offset this imbalance, local CSF accumulation may occur, potentially leading to syrinx formation.

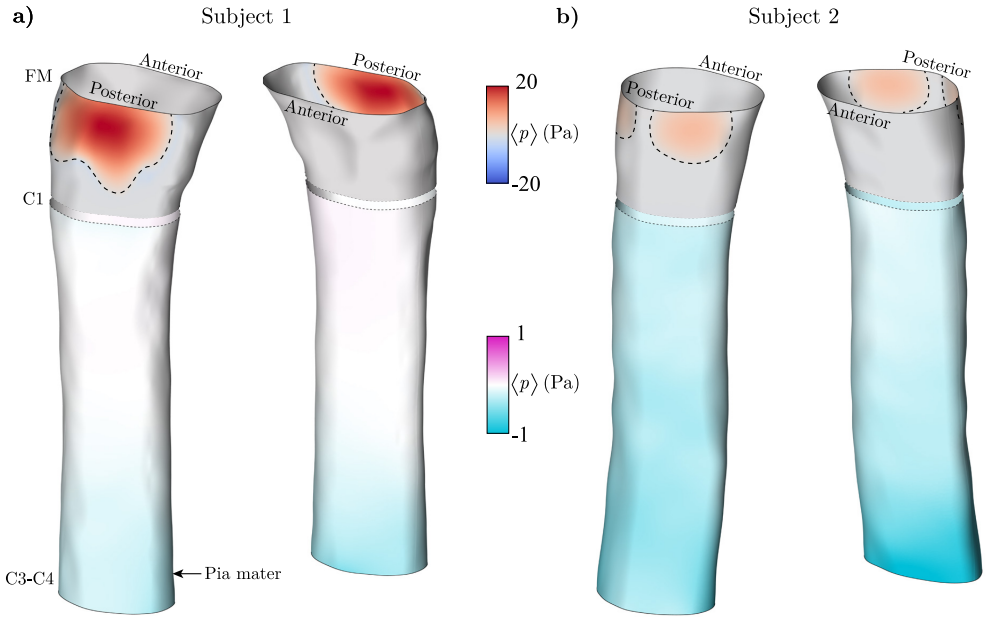

Fig. 5 Time-averaged static pressure in the craniocervical region. Spatial distribution of $\langle p \rangle$ over the pia mater for a) subject 1, who presents CM-I with associated syringomyelia, and b) subject 2, who presents CM-I without associated syringomyelia. Posterior and anterior views are shown for each subject. The dashed isocurves corresponding to $\langle p \rangle = 0.05 \langle p \rangle_{\mathrm{peak}}$ delineate the boundary of the TMF region.

Color maps are used in Fig. **??** to represent the distribution of time-averaged pressure $\langle p \rangle$, measured relative to the pressure at the FM, over the spinal-cord surface for the two subjects investigated here. Because of the marked disparity in magnitude, different scale ranges are required to visualize the pressures in the TMF, extending

from the FM to C1, and in the unobstructed SSAS, extending from C1 to C3–C4, where the pressures are smaller by more than one order of magnitude.

For the unobstructed SSAS, the fact that the time-averaged pressure, $\langle p \rangle \sim 1$ Pa, is small compared with the associated spatial and temporal pressure fluctuations, $p \sim$ tens of pascals, follows from the prevailing momentum balance. Because viscous forces and convective acceleration are negligibly small, as indicated by the order-of-magnitude estimates in Eqs. (**??**) and (**??**), the governing equation reduces, to leading order, to the linear balance given in Eq. (**??**), involving only the local acceleration and the pressure force. According to its integral form, given in Eq. (**??**), a purely periodic flow rate with $\langle Q \rangle = 0$ yields a zero time-averaged pressure gradient, consistent with the nearly uniform and very small values of $\langle p \rangle$ shown in the lower panels of Fig. **??**. Although the pressures in this region are negative when measured relative to the FM pressure, they correspond to small overpressures relative to the mean pressure at the C3–C4 level. The maximum differences are $\langle p \rangle - \langle p \rangle_{\mathrm{C3-C4}} = 0.498$ Pa for subject 1 and $\langle p \rangle - \langle p \rangle_{\mathrm{C3-C4}} = 1.151$ Pa for subject 2. These small values can be attributed to the weak nonlinear convective acceleration, which can generate a steady-streaming contribution to the time-averaged pressure, as demonstrated by Grotberg [**?**].

In contrast to the results for the unobstructed SSAS, the posterior and anterior views of the time-averaged pressure distribution within the TMF shown in Fig. **??** reveal a concentrated region of overpressure, $\langle p \rangle > 0$, centered where the cerebellar tonsils are closest to the spinal-cord surface. The isocontours $\langle p \rangle = 0.05 \langle p \rangle_{\mathrm{peak}}$ are used to delineate the approximate boundary of these pressurized regions. To understand the origin of these relatively large time-averaged pressures, it is important to note that, although the reduced momentum balance, $-\nabla p/\rho + \nu \nabla^2 \boldsymbol{v} = 0$, is linear, the flow dynamics is fundamentally nonlinear because of the deformation of the tissues bounding the squeezed film. In the FSI computations, modeled using the simple Winkler approximation given in Eq. (**??**), the local pressure modifies the thickness of the CSF film, which in turn alters its viscous resistance. During the positive-pressure phase, the central region of the film tends to dilate, whereas during the negative-pressure phase it tends to narrow. Because the hydraulic resistance depends strongly on the film thickness, the two phases of the cycle do not produce equal and opposite responses. This asymmetry rectifies the pressure oscillations, giving rise to a nonzero, predominantly positive time-averaged pressure, $\langle p \rangle$.

A comparison of subjects 1 and 2 shows that, as for the oscillatory pressure field, the spatial distribution of the time-averaged overpressure is largely determined by the tonsillar geometry. In subject 1, a single well-defined region appears as a consequence of the apparent fusion of the two tonsils. In contrast, subject 2 exhibits two distinct regions of concentrated overpressure, consistent with the tonsils remaining clearly separated.

The two subjects also exhibit marked differences in both the magnitude and spatial extent of the TMF overpressure. In subject 1, who presents CM-I with associated syringomyelia, the time-averaged overpressure reaches a peak value $\langle p \rangle_{\mathrm{peak}} = 19.38$ Pa, whereas in subject 2, who presents CM-I without syringomyelia, the corresponding peak value is only $\langle p \rangle_{\mathrm{peak}} = 6.05$ Pa. Because the effect of the TMF overpressure

on transmedullary flow depends not only on its peak magnitude but also on the surface area over which it acts, it is useful to consider the surface integral $\int_{\mathrm{TMF}} \langle p \rangle \, \mathrm{d}A$. Using the isocontour $\langle p \rangle = 0.05 \, \langle p \rangle_{\mathrm{peak}}$ to define the approximate boundary of the pressurized TMF region, this quantity yields $\int_{\mathrm{TMF}} \langle p \rangle \, \mathrm{d}A = 9.15$ Pa·cm^2 for subject 1 and 1.315 Pa·cm^2 for subject 2, corresponding to a nearly sevenfold difference. These results indicate that the alteration of transmedullary flow induced by the elevated TMF pressure may be considerably larger in subject 1, potentially providing a hydrodynamic contribution to the development of syringomyelia in this case.

3.3 Transmedullary periarterial inflow induced by tonsillomedullary-film overpressures

In healthy subjects, bidirectional transmedullary flow exhibits an approximate balance between inflow, occurring predominantly along the perivascular spaces surrounding arteries, and the accompanying outflow, occurring predominantly along perivenous spaces [**?**]. Disruption of this balance may lead to CSF accumulation within the spinal cord and ultimately to syrinx formation [**? ? ? ? ?**]. To assess the possible effect of the net overpressures generated in the TMF on transmedullary flow in patients with CM-I, it is useful to compare the resulting periarterial inflow rate with previous estimates of the pumping rate driven by the relative timing of the arterial and SSAS pressure waves [**? ? ?**].

Following [**? ? ?**], we consider the flow through a single periarterial element, modeled as a coaxial annular canal of length $\ell = 500$ μm, inner radius $R_i = 25$ μm, and outer radius $R_o = 50$ μm. Previous estimates of the resulting mass flow rate, $\dot{m}$, differ between healthy subjects and patients with CM-I and depend strongly on the phase difference between the arterial waveform and the transmedullary pressure difference. Using experimentally measured arterial phase lags, Lloyd et al. [**?**] obtained net pumping rates of $\dot{m}_{\mathrm{healthy}} \sim 0.6$ μg/s in healthy subjects (see Fig. 6 in [**?**]), which would be balanced by a corresponding outflow through the perivenous spaces. For patients with CM-I, the predicted values varied with the presence of a syrinx: $\dot{m}_{\mathrm{CM-I}} \sim 0.6$ μg/s for patients with syringomyelia and $\dot{m}_{\mathrm{CM-I}} \sim 1.6 \, \mu$g/s for those without. For the individual perivascular element, the incremental pumping rate associated with CM-I is therefore at most of order $\dot{m}_{\mathrm{CM-I}} - \dot{m}_{\mathrm{healthy}} \sim 1$ μg/s.

For the same periarterial element, the application of a steady pressure difference Δp between its two ends yields the mass flow rate

$$\dot{m} = \frac{\pi \Delta p}{8 \nu \ell} \left[R_o^4 - R_i^4 - \frac{\left(R_o^2 - R_i^2 \right)^2}{\ln \left(R_o / R_i \right)} \right]. \tag{14}$$

The resulting value depends linearly on the pressure difference applied across the periarterial element. For instance, taking $\Delta p = 10$ Pa as representative of the time-averaged overpressure in the TMF of subject 1 yields $\dot{m} \simeq 8.85$ μg/s, significantly larger than the predicted increments $\dot{m}_{\mathrm{CM-I}} - \dot{m}_{\mathrm{healthy}} \sim 1$ μg/s induced by the synchronized interaction of the arterial and SSAS pressure waves in the SSAS caudal to the tonsils [**?**].

It is worth noting that, within the TMF region, perivascular pumping can be expected to result primarily from the elevated time-averaged pressure, $\langle p \rangle$. The contribution arising from the synchronized interaction between the arterial and SSAS pressure fluctuations is comparatively small because, as shown in Figs. **??**b and **??**b, the latter are significant only during the short interval $-0.1 < t/T < 0.1$. Over this interval, the changes in the arteriolar radius, R_i, are small, thereby limiting the potential interaction between the cross-sectional-area variation and the SSAS pressure fluctuations.

3.4 Potential role of tonsillomedullary-film overpressure in the pathogenesis of syringomyelia

Our flow-rate estimates based on a previously proposed periarterial-space model [**? ? ?**] indicate that TMF overpressures may drive substantial periarterial inflow into the spinal cord, with rates approximately one order of magnitude larger than those predicted for healthy subjects, $\dot{m}_{\mathrm{healthy}} \sim 0.6$ μg/s [**?**]. Because the associated radial pressure gradient drives the flow inward, this increased transmedullary inflow cannot be balanced locally by an opposing outflow through the perivenous spaces. The CSF entering the spinal cord at the level of the TMF must therefore be evacuated longitudinally.

The CSF within the TMF compresses the spinal-cord tissue, thereby partially transmitting the external overpressure to the cord interior. Consequently, at the level of the TMF, the pressure within the spinal cord is expected to be elevated relative to more distant caudal and rostral locations. The resulting longitudinal pressure gradients may promote bidirectional CSF evacuation, both along the central canal and through the spinal-cord parenchyma. CSF moving rostrally may ultimately discharge into the fourth ventricle, whereas the fate of the caudally directed flow depends on the balance among perivenous radial outflow, central-canal flow, and longitudinal transport through the parenchyma. In some cases, radial evacuation may be sufficient to restore the global balance between transmedullary inflow and outflow. In others, the available removal pathways may be unable to accommodate the excess inflow, leading to local CSF accumulation at a more caudal location and potentially to syrinx formation. The location of this accumulation may vary among patients. In some cases, the cavity forms in close proximity to the TMF, as illustrated, for example, by the upper-cervical syrinxes reported in [**? ? ?**] and by the sagittal images provided in the Supplementary Material (Additional file 2). In other patients, CSF may accumulate at a more distant caudal location, as occurs in subject 1.

The resulting cavity, continuously supplied by longitudinal CSF flow originating at the TMF level, would be expected to maintain a slight overpressure relative to the surrounding SSAS. This pressure difference could support local perivenous outflow, allowing a quasi-steady balance to be established at a finite syrinx volume. Within this proposed scenario, the syrinx would be expected to regress once the longitudinal CSF supply is interrupted by the elimination of the TMF overpressure following surgical decompression.

The mechanistic model proposed above is intended as a plausible contributor to syrinx formation in some cases, complementing rather than replacing other explanations. As in theories based on alterations of the pressure wave in the SSAS caudal to the tonsils, the root cause of the transmedullary-flow imbalance is the cyclic motion of the cerebellar tonsils. Unlike previous theories that focus primarily on the syrinx location, however, the present model proposes that the principal changes in CSF pressure occur at the level of the TMF, where the resulting local transmedullary-flow imbalance drives longitudinal caudal transport within the spinal cord. In this respect, the present ideas are related to those of early investigators [**? ?**], who proposed that CSF enters the syrinx through the central canal as a consequence of craniospinal pressure dissociation.

3.5 Limitations of the CFD study

Our *in vivo*-informed CFD analyses of craniocervical pressure distributions in patients with CM-I have revealed several important features that may influence the inception and development of syringomyelia, including pronounced pressure fluctuations and a significant net overpressure within the TMF separating the cerebellar tonsils from the spinal cord. Additional computations involving a larger cohort of patients with and without syringomyelia, including both preoperative and postoperative cases, are needed to refine the quantification of this phenomenon and assess intersubject variability. The accuracy of the CFD simulations could also be improved through the use of more precise imaging data to prescribe tonsillar motion and CSF flow. Although the spatial and temporal resolution of the 3-T MRI and PC-MRI acquisitions was sufficient for the present study, two-dimensional PC-MRI provides only the through-plane velocity component. Higher-quality acquisitions, potentially including 7-T MRI and three-dimensional velocity measurements, could therefore improve the characterization of the computational boundary conditions. Because the induced overpressures are inversely proportional to the square of the squeezed-film thickness, as shown in Eq. (**??**), accurate determination of the tonsillar displacement during the near-contact phase of the cycle will be particularly important for ensuring the reliability of future computations. In addition, although the Winkler law adopted for the FSI modeling—which assumes that the squeezed-film overpressure is linearly proportional to the local tissue deformation—was sufficient to demonstrate the key role of compliance as a nonlinear mechanism generating net overpressures within the TMF, future work should incorporate more complete descriptions of the FSI problem that account for the three-dimensional stress and strain fields within the spinal cord and cerebellar tonsils.

4 Concluding remarks and future prospects

The present study used *in vivo*-informed CFD simulations to investigate the pressure dynamics generated by cyclic tonsillar motion in two pediatric patients with CM-I. In addition to confirming the piston-induced pressure wave in the unobstructed SSAS, the computations revealed much larger pressure fluctuations within the thin CSF film separating the moving tonsils from the spinal cord and, importantly, a nonzero time-averaged overpressure arising from the nonlinear interaction between squeeze-film

flow and tissue compliance. This overpressure was substantially larger in the subject with syringomyelia and was estimated to generate periarterial inflow rates exceeding those associated with previously proposed arterial–SSAS pumping mechanisms. These findings suggest a complementary mechanism of syrinx formation in which localized transmedullary inflow near the tonsillar level drives longitudinal CSF transport within the spinal cord and, when the available drainage pathways are insufficient, leads to fluid accumulation at a more caudal location.

Our work did not account for several physiological mechanisms that may influence the proposed explanation of syringomyelia pathogenesis, including respiration, arterial and venous pulsations, transmantle pressure gradients, tissue permeability, and possible variations in brain and spinal-cord stiffness [**? ? ? ? ?**]. These factors may determine whether the forcing associated with tonsillomedullary-film overpressure is sufficient to promote progressive syrinx enlargement in a given subject.

Future work should also seek experimental validation of the proposed mechanism. Recent animal studies have artificially altered transmedullary CSF circulation by narrowing the spinal canal [**? ? ? ?**]. Such approaches could provide a basis for future animal models combining induced Chiari malformation with the injection and tracking of an intrathecal tracer to determine whether, in selected cases, the resulting tracer pathways follow the dynamics proposed here.

Abbreviations

CM-I: Chiari malformation type I; CSF: cerebrospinal fluid; SSAS: spinal subarachnoid space; MRI: magnetic resonance imaging; ICP: intracranial pressure; FM: foramen magnum; CFD: computational fluid dynamics; PC-MRI: phase-contrast magnetic resonance imaging; FSI: fluid–tructure interaction; IRB: Institutional Review Board; SIMPLE: Semi-Implicit Method for Pressure-Linked Equations; IBM: immersed-boundary method; TMF: tonsillomedullary film.

Declarations

- Ethics approval and consent to participate: All experimental procedures were approved by the University of Utah and Intermountain Institutional Review Boards (IRB_00178613). Prior to participation, written informed consent was obtained from the parents or legal guardians of both subjects, and assent was obtained from both subjects. The study was conducted in accordance with the relevant guidelines and regulations.
- Consent for publication: All authors have approved the manuscript submission. The content of this manuscript has not been published or submitted for publication elsewhere.
- Availability of data and materials: The raw data are available from the corresponding author on reasonable request.
- Competing interests: The authors declare that they have no competing interests.
- Funding: The work at UC San Diego and Primary Children's Hospital was supported by the American Syringomyelia Alliance Project, Inc. through the project Validating an Analytic Model for Cerebrospinal Fluid Flow Across the Foramen Magnum in

Children with Chiari I Malformation with Syringomyelia: A Study of Patients Before and After Surgery. The work at the University of Jaén, the University of Granada, and Universidad Carlos III de Madrid was supported by the coordinated project PID2023-151343NB-C31, PID2023-151343NB-C32, and PID2023-151343NB-C33, financed by MICIU/AEI/10.13039/501100011033 and by FEDER, UE.

- Authors' contributions: Conceptualization: FJP-M, GLN, VMR, CG-M, ALS; Methodology: FJP-M, GLN, WC, CM-B, CG-M, ALS; Investigation: FJP-M, GLN, MSz, WC, CM-B, VMR, AL, MSp, JR, DB, CG-M, ALS; Interpretation: FJP-M, GLN, WC, CM-B, CG-M, ALS; Supervision: CG-M, ALS; Writing–original draft: FJP-M, GLN, CG-M, ALS; Writing–review & editing: FJP-M, GLN, MSz, WC, CM-B, VMR, AL, MSp, JR, DB, CG-M, ALS
- Acknowledgements: Not applicable.
- Authors' information: [1] Área de Mecánica de Fluidos, Departamento de Ingeniería Mecánica y Minera, Universidad de Jaén, Jaén, 23071, Spain. [2] Department of Mechanical and Aerospace Engineering, University of California San Diego, La Jolla, CA 92093-0411, USA. [3] Departamento de Ingeniería Térmica y de Fluidos, Universidad Carlos III de Madrid, Leganés, 28911, Spain. [4] Área de Mecánica de Fluidos, Departamento de Mecánica de Estructuras e Ingeniería Hidráulica, Universidad de Granada, Granada, 18071, Spain. [5] Division of Pediatric Neurosurgery, Primary Children's Hospital, Salt Lake City, UT, 84113, USA. [6] Andalusian Institute for Earth System Research, Universidades de Granada, Córdoba y Jaén. Avenida del Mediterráneo s/n, Granada, 18006, Spain.

Supplementary Information.

- **Name of File: FSI validation**
- **Format: pdf**
- **Title: Additional File 1**
- **Description: Comparison between the numerical predictions of the pressure field and wall deformation in a geometrically simple, compliant squeeze-film configuration with the corresponding quasi-analytical predictions of lubrication theory.**

- **Name of File: T2 images**
- **Format: Word**
- **Title: Additional File 2**
- **Description: T2-weighted MRI images of CM-I patients presenting with upper-cervical syrinxes.**